NUREG/CR-3980 Vol. I
ANL-84-61 Vol. I

NUREG/CR-3980 Vol. I
ANL-84-61 Vol. I

LIGHT-WATER-REACTOR SAFETY FUEL SYSTEMS RESEARCH PROGRAMS: QUARTERLY PROGRESS REPORT

January – March 1984

ARGONNE NATIONAL LABORATORY, ARGONNE, ILLINOIS
Operated by THE UNIVERSITY OF CHICAGO

Prepared for the Office of Nuclear Regulatory Research
U. S. NUCLEAR REGULATORY COMMISSION
under Interagency Agreement DOE 40-550-75

Argonne National Laboratory, with facilities in the states of Illinois and Idaho, is owned by the United States government, and operated by The University of Chicago under the provisions of a contract with the Department of Energy.

NUREG/CR-3980 Vol. I
ANL-84-61 Vol. I

Distribution
Code: R3

ARGONNE NATIONAL LABORATORY
9700 South Cass Avenue
Argonne, Illinois 60439

LIGHT-WATER-REACTOR SAFETY FUEL SYSTEMS RESEARCH PROGRAMS: QUARTERLY PROGRESS REPORT

January—March 1984

Date Published: September 1984

Previous reports in this series

ANL-83-85 Vol. I	January—March 1983
ANL-83-85 Vol. II	April—June 1983
ANL-83-85 Vol. III	July—September 1983
ANL-83-85 Vol. IV	October—December 1983

Prepared for the Division of Accident Evaluation
Office of Nuclear Regulatory Research
U. S. Nuclear Regulatory Commission
Washington, D. C. 20555
Under Interagency Agreement DOE 40-550-75

NRC FIN Nos. A2016 and A2017

LIGHT-WATER-REACTOR SAFETY
FUEL SYSTEMS RESEARCH PROGRAMS
QUARTERLY PROGRESS REPORT

January-March 1984

ABSTRACT

This progress report summarizes work performed by the Materials Science and Technology Division of Argonne National Laboratory during January, February, and March 1984 on water reactor safety problems related to fuel and cladding. The research and development areas covered are Transient Fuel Response and Fission Product Release and Clad Properties for Code Verification.

NRC Fin No.	FIN Title
A2016	Transient Fuel Response and Fission Product Release
A2017	Clad Properties for Code Verification

TABLE OF CONTENTS

Page

EXECUTIVE SUMMARY.....iv

I. TRANSIENT FUEL RESPONSE AND FISSION PRODUCT RELEASE.....1

A. Description of FASTGRASS-VFP Theory.....1

B. Fission Product Behavior in High-Burnup Fuel during ORNL In-Cell Heating Tests.....8

C. Fission Product Behavior in Trace-irradiated Fuel during SFD Tests in the PBF Reactor.....12

D. Conclusions.....20

E. References for Chapter I.....21

II. CLAD PROPERTIES FOR CODE VERIFICATION (H. M. Chung, F. L. Yaggee, and T. F. Kassner).....23

A. Observation of Zr_3O Precipitates on Dislocation Substructures.....24

1. Introduction.....24

2. s-parameter of the Big Rock Point Cladding Specimen 165AE4B.....25

B. References for Chapter II.....36

LIGHT-WATER-REACTOR SAFETY
FUEL SYSTEMS RESEARCH PROGRAM:
QUARTERLY PROGRESS REPORT

January-March 1984

EXECUTIVE SUMMARY

I. TRANSIENT FUEL RESPONSE AND FISSION PRODUCT RELEASE[a]

The theoretical FASTGRASS-VFP model has been used in the interpretation of fission gas, iodine, and cesium release from (1) irradiated high-burnup LWR fuel in a flowing steam atmosphere during high-temperature, in-cell heating tests performed at Oak Ridge National Laboratory and (2) trace-irradiated LWR fuel during severe-fuel-damage (SFD) tests performed in the PBF reactor in Idaho. A theory of grain boundary sweeping of gas bubbles has been included within the FASTGRASS-VFP formalism. This theory considers the interaction between the moving grain boundary and two distinct size classes of bubbles, those on grain faces and on grain edges, and provides a means of determining whether gas bubbles are caught up and moved along by a moving grain boundary or whether the grain boundary is only temporarily retarded by the bubbles and then breaks away. The results of the analyses demonstrate that intragranular fission product behavior during both types of tests can be interpreted in terms of a grain-growth/grain-boundary-sweeping mechanism that enhances the low of fission products from within the grains to the grain boundaries. The FASTGRASS-VFP predictions, measured release rates from the above tests, and previously published release rates are compared and differences between fission product behavior in trace-irradiated and in high-burnup fuel are highlighted.

---

[a]RSR FIN Budget No. A2016; RSR Contact: L. Chan.

II. CLAD PROPERTIES FOR CODE VERIFICATION[b]

Zircaloy fuel cladding is susceptible to local breach-type failures during power transients in LWRs because of stresses imposed by differential thermal expansion of the fuel and cladding. In this program, the effect of stress state, strain rate, and temperature on the deformation characteristics of irradiated Zircaloy fuel cladding is being investigated to provide mechanical-property information and a failure criterion for the cladding under loading conditions conducive to pellet-cladding interaction (PCI). The information will be used in the development of codes to analyze PCI in fuel rods from power ramp experiments in test reactors, and to evaluate the susceptibility of extended-burnup fuel elements and new fuel element designs in commercial reactors to PCI failures during power transients.

Continued efforts in the TEM-HVEM examination of the brittle-type PCI-like failure produced in Big Rock Point fuel cladding by internal gas pressurization at 325°C resulted in a direct observation of individual dislocations decorated by Zr_3O precipitates. This provides further evidence that brittle-type failures are associated with segregation of oxygen (present in the cladding material either as an alloying element or as a by-product of in-reactor corrosion) to dislocations and radiation-induced defects, which leads to the formation of a Zr_3O phase, an immobilization of dislocations, and eventually to a minimal plastic deformation in the material. A large number of diffraction patterns were obtained from dislocation substructures of Big Rock Point cladding that failed in a brittle manner and the patterns were analyzed for the Zr_3O superlattice reflections. From an analysis of the results, the fraction of the number of diffraction patterns that contained the superlattice reflections was determined and the fraction was denoted as the s-parameter. The s-parameter provides a quantitative measure of the extent of the Zr_3O phase precipitation on and immobilization of dislocations in the specimen. The value of the parameter was 0.62 for a specimen that failed in a brittle manner and exhibited a large extent of the pseudocleavage plus fluting feature (characteristic of a pellet-cladding interaction failure) on the fracture surface. The parameter had a value of 0.09 for a specimen that failed in a ductile manner.

---

[b]RSR FIN Budget No. A2017; RSR Contact: H. H. Scott.

I. TRANSIENT FUEL RESPONSE AND FISSION PRODUCT RELEASE

Principal Investigator:
J. Rest

A. Description of FASTGRASS-VFP Theory

FASTGRASS-VFP[1-3] is a mechanistic computer model for predicting the behavior of fission gas and volatile fission products (VFPs) in solid UO_2-based fuels during steady-state and transient conditions. The model accounts for the effects of a number of processes on both the distribution of fission products within the fuel and the amount released. These processes include fission product generation; gas bubble nucleation and resolution; bubble migration and coalescence; interaction between I, Cs, CsI, and fission gas bubbles; chemical reaction between I, Cs, and fuel; channel formation on grain faces; interlinked porosity on grain edges; and microcracking. The present version of the theory models the fission gases Xe and Kr; the volatiles I and Cs; and the major VFP reaction products, CsI, Cs_2MoO_4, and Cs_2UO_4. Including the latter two reaction products can alter the Cs and CsI release predictions by up to 10%.[2] Fission products released from the fuel are assumed to reach the pellet surface by successively migrating from the grain interiors to grain faces and then to the grain edges, with subsequent transport through a network of interconnected tunnels and as-fabricated porosity.

The approach to modeling VFP chemistry in FASTGRASS-VFP is to assume that the kinetics of the relevant reactions occur fast enough for a quasi-equilibrium to be maintained. The following reactions are considered to dominate I and Cs release characteristics:

$$C_s + I \longrightarrow CsI;\quad 2Cs + UO_2 + O_2 \longrightarrow Cs_2UO_4;\ \text{and}\ 2Cs + Mo + 2O_2 \longrightarrow Cs_2MoO_4.$$

The model for the VFP chemistry is based on the analysis of Tam et al., which employs the laws of mass balance and mass action.[4]

FASTGRASS-VFP has recently been used[5] in the interpretation of fission gas, iodine, and cesium release from (1) irradiated high-burnup LWR fuel in a flowing steam atmosphere during high-temperature, in-cell heating tests performed at Oak Ridge National Laboratory (ORNL) and (2) trace-irradiated LWR fuel during severe-fuel-damage (SFD) tests performed in the PBF Reactor in Idaho. The results of these analyses demonstrated that intragranular fission product behavior during both types of tests can be interpreted in terms of a grain-growth/grain-boundary-sweeping mechanism that enhances the flow of fission products from within the grains to the grain boundaries. Basically, the model assumes that small intragranular bubbles (consisting, in general, of Xe, Kr, I, Cs, and CsI), and gaseous and VFP atoms in the path of a growing grain, are swept up by grain boundary adhesive forces. Such grain boundary sweeping provides another mechanism for the collection of fission products at grain faces and edges. The grain growth model employed in Ref. 5 is limited in that it depends only on temperature and does not include the retarding effects of bubbles being swept along by the moving grain boundary.

A theory of grain boundary sweeping of gas bubbles has been included within the FASTGRASS-VFP formalism. This theory considers the interaction between the moving grain boundary and two distinct size classes of bubbles, those on grain faces and on grain edges, and provides a means of determining whether gas bubbles are caught up and moved along by a moving grain boundary or whether the grain boundary is only temporarily retarded by the bubbles and then breaks away.

At temperatures of about 1900 K,[6] atomic mobilities in UO_2 result in an enhanced migration of atoms from the convex to the concave side of a curved boundary. The atoms move toward the concave side of the boundary because in that location, they are surrounded by a somewhat larger number of neighboring atoms and thereby exhibit a lower effective energy state. The net result of this atomic motion is shrinkage of small grains with predominantly convex surfaces and growth of larger grains with concave surfaces.

Speight and Greenwood[7] have proposed a grain growth theory which includes the sweeping of entrapped microbubbles by the front of an advancing grain boundary. The basic postulate of their theory is that small bubbles exert a minimal drag force on an advancing grain surface and thus are swept along with the moving boundary, while large bubbles detach from the advancing surface because of their higher drag. To assess the efficiency of bubble sweeping, they compared the magnitude of the force exerted by a bubble on the boundary, i.e.,

$$F_b = \pi R_b \gamma_{gb} \sin 2\phi \quad , \tag{1.1}$$

with the adhesive effects of the interfacial surface tensions, i.e.,

$$F_{gb} \simeq \frac{2\gamma_{gb}}{r_c} \pi r_{gb}^2 \quad , \tag{1.2}$$

where R_b = bubble radius, r_c = radius of curvature of the grain, r_{gb} = characteristic distance of bubble spacing, γ_{gb} = grain boundary surface tension, and ϕ = angle of contact between the bubble and the boundary.

Whereas Speight and Greenwood considered the effects of the moving boundary interacting with a population of equal-sized bubbles, the present theory includes the effects on the moving boundary of two distinct distributions of bubble sizes, those on the grain faces and those on the grain edges. In addition, as FASTGRASS-VFP provides for a mechanistic calculation of intra- and intergranular fission product behavior, the coupled calculation between fission gas behavior and grain growth is kinetically comprehensive. The magnitude of the force exerted by the bubbles on the boundary, or vice versa, depends on bubble radius and angle of contact according to the relationship

$$F_b = \pi R_F \gamma_{gb} \sin 2\phi_F + \pi R_E \gamma_{gb} \sin 2\phi_E \quad , \tag{1.3}$$

where R_F and R_E are the bubble radii for grain face and grain edge bubbles, respectively, and ϕ_F and ϕ_E are the corresponding angles of contact between the bubbles and the boundary.

Assuming that the grain face and grain edge bubbles move by surface diffusion control, the velocity of these bubbles can be expressed as

$$V_F = \frac{3}{4} \frac{a_o^4 D_o}{R_F^3} \left(\frac{2\gamma_{gb}}{KT} \right) \sin 2\phi_F \exp\left(\frac{-E_s}{KT} \right), \tag{1.4}$$

and

$$V_E = \frac{3}{4} \frac{a_o^4 D_o}{R_E^3} \left(\frac{2\gamma_{gb}}{KT} \right) \sin 2\phi_E \exp\left(\frac{-E_s}{KT} \right), \tag{1.5}$$

where V_F and V_E are the velocities of the face and edge bubbles, respectively, a_o is the lattice constant, T is the absolute temperature, K is Boltzmann's constant, D_o is the preexponential factor for surface self-diffusion of the matrix solid, and Es is the activation energy for this process.

In order to determine the contact angles ϕ_F and ϕ_E in Eqs. (1.4) and (1.5), the velocity of the moving grain boundary needs to be evaluated. The net flux of atoms, J, across a curved grain boundary occurs because the binding energy of the atoms in the matrix is somewhat higher on the concave than on the convex side of the boundary. The net flux of atoms across the boundary can be expressed as

$$J = \frac{\nu}{a_o^2} \frac{\Delta E}{KT} \exp(-Q/KT), \tag{1.6}$$

where ν is the frequency of vibration of an atom in the solid lattice adjacent to the boundary, Q is the activation energy for grain boundary motion, and ΔE is the difference in energy between atoms located on the concave versus the convex side of the boundary. The velocity of the grain boundary, V_{gb}, is the product of the flux J and the atomic volume, which is approximately equal to the cube of the lattice constant:

$$V_{gb} = \Omega a_o^3 = \nu a_o \frac{\Delta E}{KT} \exp(-Q/KT). \tag{1.7}$$

The energy difference ΔE can be related to the intrinsic properties of the curved grain boundary and to the sizes and numbers of gas bubbles

attached to the boundary. In the absence of differential strain between adjacent grains, the intrinsic grain-boundary tension force is the primary force acting on the boundary, and acts to move the boundary toward the center of curvature of the convex grain. The grain face and grain edge bubbles exert a drag force in the opposite direction. If a section of grain boundary with area A_{gb} moves a distance dx, the change in energy is

$$\left[\frac{2\gamma_{gb}}{r_c}\left(A_{gb}\right) - F_b\right] dx,$$

where F_b is given by Eq. (1.3). The number of atoms displaced from one side of the boundary to the other is

$$\frac{A_{gb}\,dx}{a_o^3}.$$

Dividing this expression by the preceding one gives the energy change per atom transferred across the boundary, ΔE:

$$\Delta E = \frac{2a_o^3}{r_c}\left(1 - \frac{\pi R_F r_c \sin 2\phi_F}{A_{gb}} - \frac{\pi R_E r_c \sin 2\phi_E}{A_{gb}}\right). \tag{1.8}$$

Inserting Eq. (1.8) into Eq. (1.7) yields the grain boundary velocity

$$V_{gb} = \frac{2a_o^4\, 2\gamma_{gb}}{r_c KT} \exp\left(-Q/KT\right)\left[1 - 1/2\left(\frac{\pi R_F^2}{A_{gb}}\right)\left(\frac{r_c}{R_F}\right)\sin 2\phi_F - 1/2\left(\frac{\pi R_E^2}{A_{gb}}\right)\left(\frac{r_c}{R_E}\right)\sin 2\phi_E\right]. \tag{1.9}$$

When the bubbles are widely spaced or very small, the second and third terms in the brackets in Eq. (1.9) are negligible compared to unity, and V_{gb} reduces to the intrinsic velocity of the curved grain boundary. The second and third terms in the brackets in Eq. (1.9) account for the retarding effects of the bubbles on grain boundary motion.

If both the grain face and grain edge bubbles are swept along with the moving boundary, then

$$V_F = V_E = V_{gb}. \tag{1.10}$$

The first equality in Eq. (1.10) yields

$$\frac{\sin 2\phi_F}{R_F^3} = \frac{\sin 2\phi_E}{R_E^3} . \tag{1.11}$$

From Eqs. (1.9-1.11), one obtains

$$\sin 2\phi_E = \left[\frac{3}{4} \frac{D_o r_c}{R_E^3 \nu} \exp -\left(\frac{E_s - Q}{KT}\right) + 1/2 \left(\frac{\pi R_E^2}{A_{gb}}\right)\left(\frac{r_c}{R_E}\right) + 1/2 \left(\frac{\pi R_F^2}{A_{gb}}\right)\left(\frac{r_c}{R_F}\right)\left(\frac{R_F}{R_E}\right)^3 \right]^{-1} \tag{1.12}$$

Since sin 2ϕ cannot exceed unity, the condition for bubble detachment is met when the right hand side of Eq. (1.12) exceeds unity. If this condition is satisfied and $R_F = R_E$, both face and edge bubbles become detached from the boundary. If $R_F \neq R_E$, the larger bubble becomes detached (we assume for the sake of this discussion that $R_E > R_F$) and the condition that the smaller bubble be swept along with the moving boundary is examined by requiring

$$V_F = V_{gb},$$

which results in

$$\sin 2\phi_F = \left[\frac{3}{4} \frac{D_o r_c}{R_F^3 \nu} \exp\left(- \frac{Es - Q}{KT}\right) + 1/2 \left(\frac{\pi R_F^2}{A_{gb}}\right)\left(\frac{r_c}{R_F}\right) \right]^{-1} . \tag{1.13}$$

If the right hand side of Eq. (1.13) exceeds unity, then the smaller bubble (R_F in this case) is also detached from the boundary. If the right hand side of Eq. (1.12) or (1.13) is less than unity, both face and edge bubbles, or just face bubbles, respectively, are swept along with the moving boundary. The contact angles ϕ_F and ϕ_E can be computed from Eqs. (1.11-1.13) and used in Eqs. (1.4) and (1.5) or (1.9) to determine the bubble or grain boundary velocity.

Fuel stoichiometry can have a pronounced effect on atomic mobilities in UO_2 fuel and thus on grain growth kinetics. Data[8] on the diffusivity of ^{133}Xe in UO_{2+x} as a function of fuel stoichiometric condition show that increased levels of oxygen in solution in UO_2 lead to observed increases in the diffusivity of ^{133}Xe and ^{85}Kr. For example, a change from $UO_{2.0}$ to

$UO_{2.12}$ can increase the diffusivity of ^{133}Xe by more than two orders of magnitude. Thus, the stoichiometry of the oxide can have a significant impact on atomic mobility and grain growth characteristics. Indeed, for the highly oxidizing environment of fuel exposed to steam flow at elevated temperatures, UO_2 can be expected to become hyperstoichiometric during the course of a severe-core-damage accident.

To account for such oxidation effects, two values of the activation energy, Q, are employed in the present version of FASTGRASS-VFP. For stoichiometric $UO_{2.00}$ (nominal grain growth), Q = 357 kJ/mole. This value of Q for stoichiometric fuel is close to the value of 360 kJ/M determined by MacEwan and Hayashi.[9] For hyperstoichiometric (oxidized) fuel, the activation energy is decreased to Q = 294 kJ/Mole, approximately proportional to the difference in activation energy between UO_2 and UO_{2+x} reported by Turnbull.[10] This value of Q was determined by the requirement that the integrated intragranular fission gas release as calculated by FASTGRASS-VFP must be consistent with measured total (end-of-test) release values for
SFD-ST.

As the boundary moves, the rate $\frac{dC_{gb}}{dt}$ at which fission products are swept up by the moving boundary is proportional to the rate of change of the volume of the grain; i.e.,

$$\frac{dC_{gb}}{dt} = \frac{\pi e C_I D_t^2}{2} \frac{dD_t}{dt} = \frac{\pi e C_I D_t^2 V_{gb}}{2} , \qquad (1.14)$$

where C_I is the intragranular concentration of a fission product, D_t is the grain diameter at time t, and e is a factor that describes the grain boundary sweeping efficiency. The factor e includes atomic vibrational and minimum energy effects. The value of e is assumed to be unity for the fission gases, I, and CsI (in bubbles), and 0.6 for atomic Cs. The lower value of e for Cs is consistent with the high chemical affinity of Cs for UO_2, other fission products, and metallic inclusions.

For each fission product, Eq. (1.14) provides one term in the overall equations for the various dC_I/dt and one term in the overall equations for

the various intergranular fission products, $\frac{dC_B}{dt}$ (e.g., see Ref. 3). The bubble radii, the intra- and intergranular concentrations of the fission products, the grain size, and the fraction of the grain boundary area occupied by bubbles ($\pi R_F^2/A_{gb}$ and $\pi R_E^2/A_{gb}$ in Eqs. 1.9, 1.12 and 1.13) are calculated as a function of time. The values employed for various quantities used in Eqs. (1.4-1.5) and (1.9-1.13) are $\nu = 1.0 \times 10^{12} s^{-1}$, $r_c = D_t/2$, $D_o = 4 \times 10^5$ cm^2/s, and $E_s = 453.6$ kJ/mole.

B. Fission Product Behavior in High-burnup Fuel during ORNL In-Cell Heating Tests

Figures. 1.1 and 1.2 show FASTGRASS-VFP predictions of fission gas and Cs release for ORNL tests HI-1 and HI-3,[11] and compare them with the corresponding measured quantities. Tests HI-1 and HI-3 were conducted for 30 min at 1673 K and 20 min at 2273 ± 50 K, respectively, within a flowing steam environment. The fuel specimens were 20-cm-long sections of H. B. Robinson fuel rod irradiated to 28,000 MWd/MTU. In order to assess correctly the state of the fuel prior to the test, a thermally and mechanically coupled model consisting of FASTGRASS-VFP and the LIFE-LWR fuel behavior code was used for the in-reactor irradiation period.[3] The total gas released during the irradiation was about 0.2%.

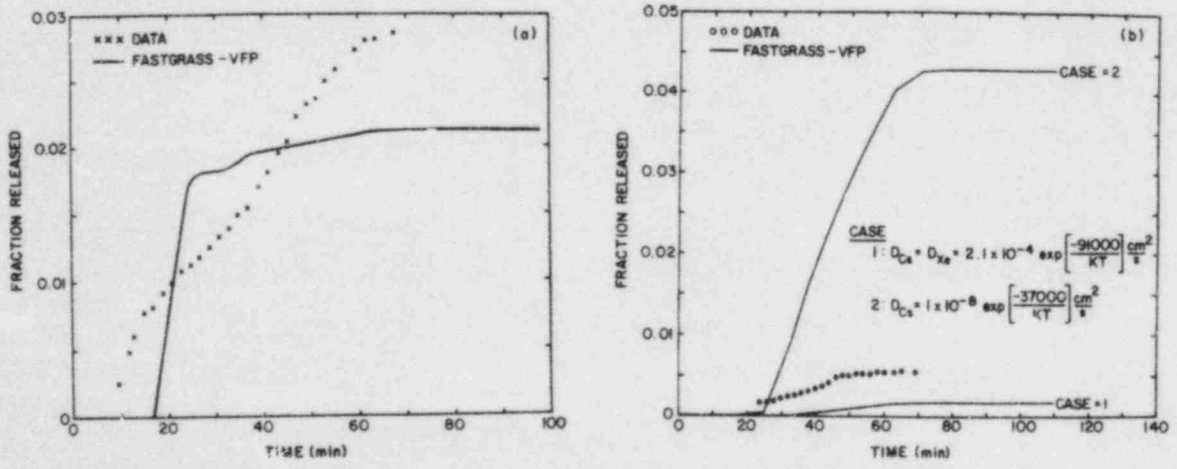

Fig. 1.1. FASTGRASS-VFP Predictions of (a) Fission Gas and (b) Cesium Release during ORNL Test HI-1, Compared with Measured Values. In (b), predictions are given for two values of the cesium diffusion coefficient.

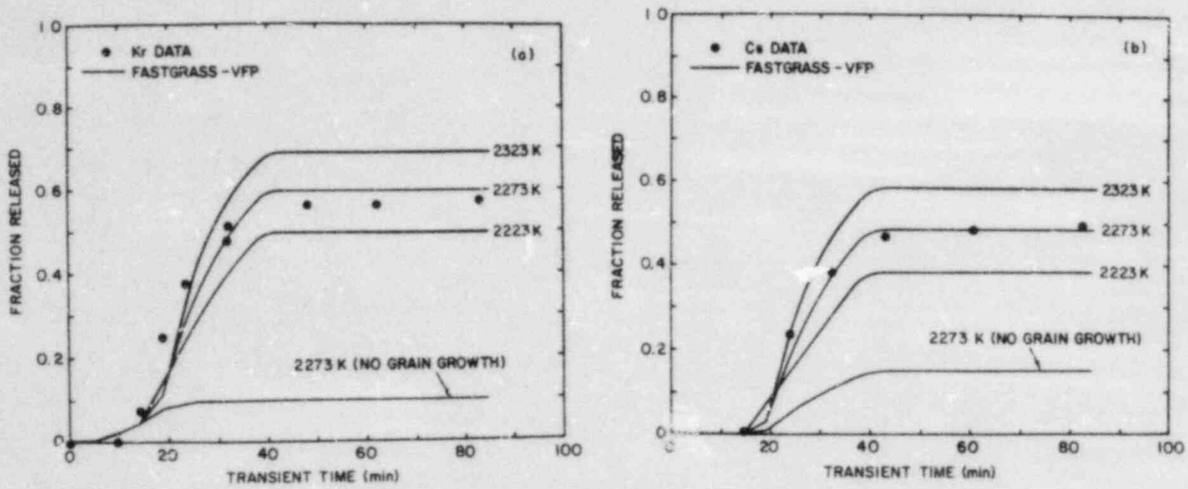

Fig. 1.2. FASTGRASS-VFP Predictions of (a) Fission Gas and (b) Cesium Release during ORNL Test HI-3, Compared with Measured Values.

The value of Q for stoichiometric $UO_{2.00}$ was used for both test simulations: This resulted in predictions of no grain growth for HI-1 and a 26-45% increase in grain size for HI-3. These grain growth predictions are consistent with microscopic observations. Figure 1.3 shows scanning electron micrographs of H. B. Robinson fuel specimens before and after test HI-3; the grain size before transient heating was approximately 4.2 μm, whereas post-test examination indicates an ~50% increase in grain size. More detailed microscopic results are presented in Ref. 12.

Very little fission gas and Cs release occurred during HI-1 (Fig. 1.1). Two curves for predicted Cs release are shown in Fig. 1.1b; these correspond to two different values of Cs diffusivity. The relatively high release predictions were based on the Cs diffusivities reported by Matzke,[13] while the low release predictions were based on the assumption that the diffusivities are the same for Cs as for Xe (D_{Xe} is based on the data of Cornell[14]). The Cs diffusivities used in earlier studies[1,2] (based on the work of Oi and Takagi, as discussed in Refs. 1 and 2) result in Cs release predictions for test HI-1 which are a factor of ~3 larger than those obtained with the diffusivities reported by Matzke. As the effects of chemical trapping are included in the FASTGRASS-VFP calculations (i.e., CsI,

Cs_2MoO_4, and Cs_2UO_4 reaction products), and as the relatively low HI-1 test temperatures preclude any appreciable grain growth, the predicted D_{Cs} dependence of fission product release during the test should be physically realistic. The results shown in Fig. 1.1b suggest that equating D_{Cs} with D_{Xe} is the most reasonable assumption. Consequently, this value of D_{Cs} is used in all subsequent calculations.

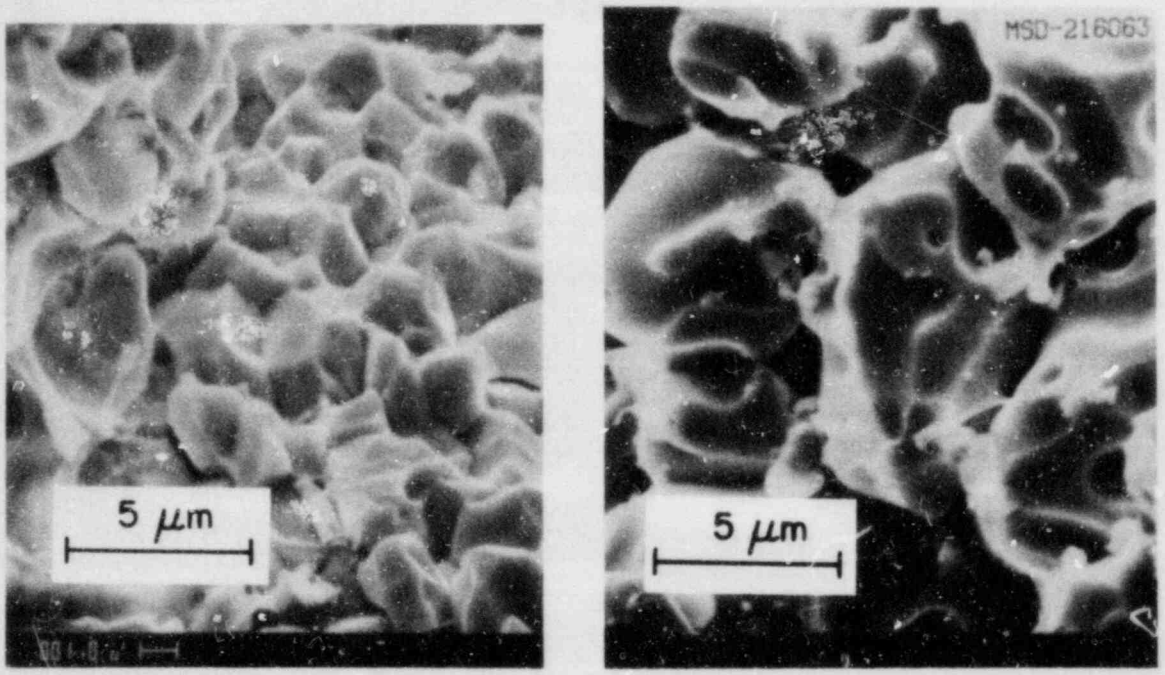

Fig. 1.3. Scanning Electron Micrographs of H. B. Robinson Fuel (left) before and (right) after ORNL Test HI-3.

In order to reflect the reported experimental uncertainty in temperature for test HI-3, each part of Fig. 1.2 includes three predicted curves, which correspond to test temperatures of 2273 ± 50 K. Also shown in Fig. 1.2 are the predictions of the theory in the absence of grain growth. On the basis of the good agreement between theory and data for fission gas and Cs release when a grain-growth/grain-boundary-sweeping mechanism is operative (Fig. 1.2), and the agreement between predicted and observed end-of-test grain size, it is concluded that grain boundary sweeping of fission products is a key mechanism for moving fission products from within the grains to the grain boundaries under HI-3 test conditions.

This position is further supported by the agreement between the FASTGRASS-VFP results for fission gas and Cs release and the data for test HI-4[11] shown in Fig. 1.4. The fuel specimen for test HI-4 consisted of a 20.3-cm-long fuel segment from a rod which had been irradiated in the Peach Bottom-2 reactor to about 10,100 MWd/MTU. Again, FASTGRASS-VFP/LIFE-LWR was used to simulate the irradiation period prior to the transient test. About 9% fission gas release occurred from this rod during the irradiation. Test HI-4 consisted of 20 min at a temperature of 2073 ± 50 K in a flowing steam-helium atmosphere. If the value of Q for stoichiometric $UO_{2.00}$ is used and an initial grain size of 6 μm is assumed, the theory predicts an ~10% increase in grain size. Again, this grain growth prediction is consistent with microscopic observations.[12]

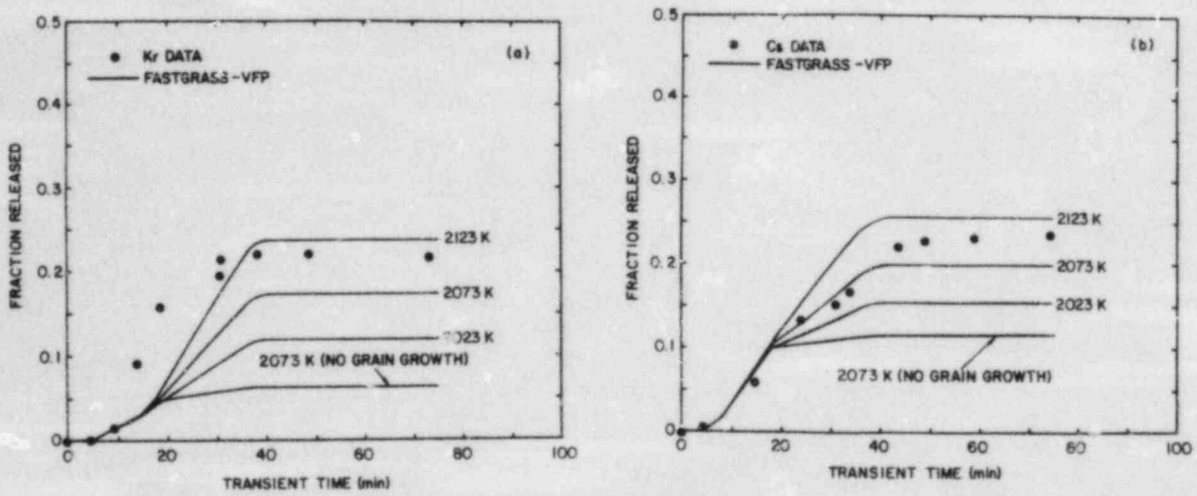

Fig. 1.4. FASTGRASS-VFP Predictions of (a) Fission Gas and (b) Cesium Release during ORNL Test HI-4, Compared with the Measured Values.

It should be noted that whereas partial oxidation of the cladding was observed after tests HI-3 and HI-4 , no visual evidence of appreciable fuel oxidation was detected.[12] This result is consistent with the use of the stoichiometric grain growth law within FASTGRASS-VFP for HI-1, HI-3, and HI-4 test conditions.

Figure 1.5 shows FASTGRASS-VFP predictions of fission gas and Cs release for test HI-2.[11] The HI-2 test specimen was similar to those used

in tests HI-1 and HI-3. Test HI-2 was conducted for 20 min at about 1973 K in flowing steam. Metallographic examination[11,12] of the tested fuel specimen revealed extensive fractures in the cladding, essentially complete oxidation to ZrO_2, and evidence of fuel-cladding interaction. Thus, it seems likely that fuel oxidation did occur during test HI-2, in contrast to tests HI-1, HI-3, and HI-4. Each part of Fig. 1.5 shows predicted curves obtained with both the stoichiometric ("nominal") grain growth activation energy (maximum fuel temperature = 1973 K) and the hyperstoichiometric ("enhanced") grain growth activation energy (maximum fuel temperature = 1973 ± 50 K), as well as the predictions of the theory for the case of no grain growth (maximum fuel temperature = 1973 K). For the cases where the hyperstoichiometric grain growth activation energy is used, the agreement between theory and data is quite good. Thus, both the experimental results available to date and the FASTGRASS-VFP analysis (Fig. 1.5) indicate that the UO_2 diffusivities were enhanced to some extent during test HI-2 owing to UO_2 oxidation to UO_{2+x}.

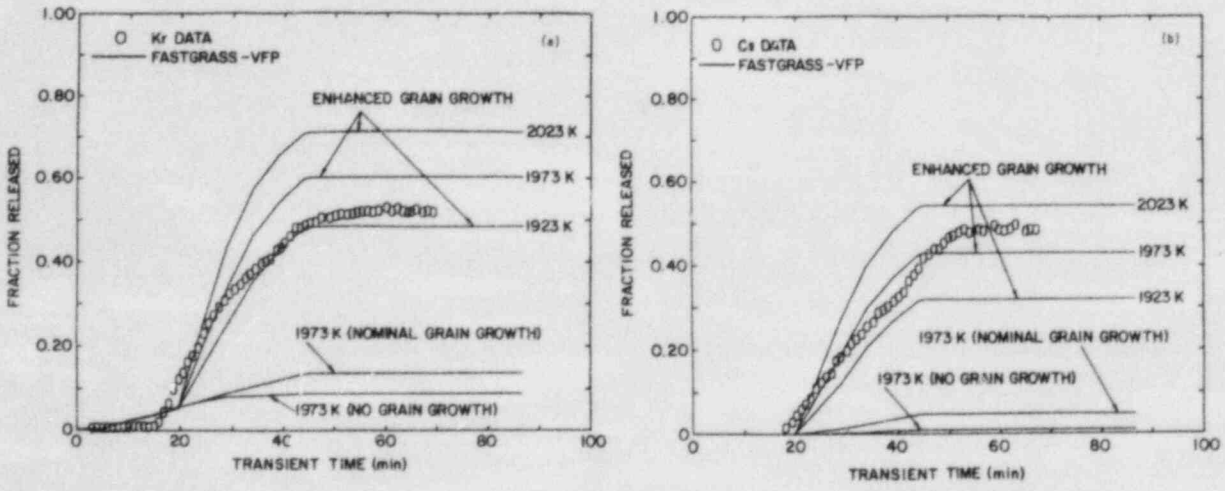

Fig. 1.5. FASTGRASS-VFP Predictions of (a) Fission Gas and (b) Cesium Release during ORNL Test HI-2, Compared with the Measured Values.

C. Fission Product Behavior in Trace-irradiated Fuel during SFD Tests in the PBF Reactor

The SFD-ST experiment[15] consisted of a 32-rod bundle of PWR-type fuel rods, 0.91 m long and enclosed in an insulated shroud. The bundle was

subjected to a slow heatup (~2 h) in an oxygen-rich environment to about 1400 K in the lower part of the fuel bundle and about 1800 K in the upper portion of the bundle and then rapid heatup (~10 min) to 2400 K, followed by a rapid quench and coolant reflood. Considerable cladding oxidation and melting, fuel liquefaction, and fuel fragmentation occurred. The SFD 1-1 test[15] also consisted of a 32-rod bundle, but the temperature transient consisted of a rapid heatup (~30 min) in a steam-starved environment to 2400 K followed by a slow cooldown (~20 min) without a rapid quench. The effective burnup levels for SFD-ST and SFD 1-1 are 88.9 and 79.1 MWd/MTU, respectively.

In Fig. 1.6, the measured fission gas release rates for SFD-ST are compared with the release rates predicted by FASTGRASS-VFP on the basis of both the stoichiometric (nominal) and hyperstoichiometric (enhanced) grain growth activation energies. The enhanced grain growth activation energy, which is assumed to be activated at the time when the peak fuel temperatures exceed 1900 K, gives rise to a release rate curve that simulates the ST data quite well, whereas the nominal value of Q gives release rates that are approximately an order of magnitude below the data at fuel temperatures >1900 K. Such differences in predicted release characteristics due to grain-growth/grain-boundary-sweeping effects are further illustrated in Fig. 1.7, which shows intragranular fission gas retention during SFD-ST as predicted by FASTGRASS-VFP. If nominal grain growth occurs, the majority of the fission gas is predicted to remain trapped within the grain interior, with a total fractional retention of greater than 80% even as fuel temperatures approach 2400 K. However, if the grain growth is enhanced owing to fuel oxidation, a much larger fraction of the intragranular gas is swept to grain boundaries, with only ~10% retention within grains at fuel temperatures of ~2400 K. Such predictions clearly illustrate the important influence of the grain-growth/sweeping process on the morphology and attendant release behavior of gaseous and volatile fission products.

Figure 1.8 shows FASTGRASS-VFP predictions of grain growth in the hottest fuel region of SFD-ST for the cases of nominal and enhanced grain growth. The theory predicts more than a twofold increase in grain size (for a 10-μm initial grain size) when the hyperstoichiometric grain growth

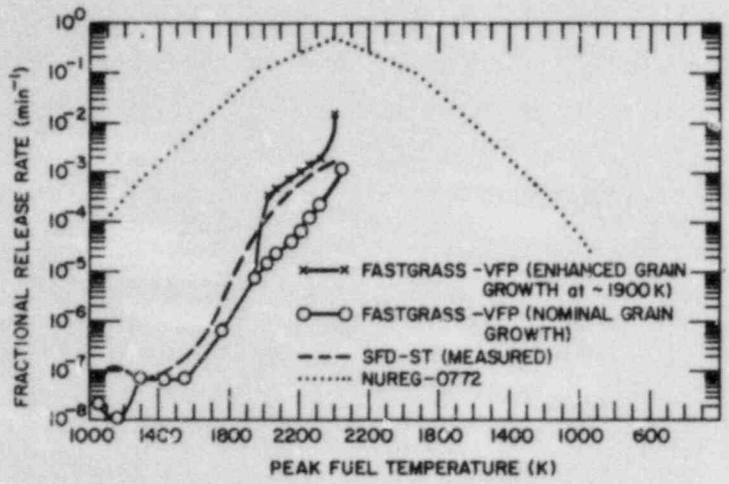

Fig. 1.6.

FASTGRASS-VFP Predictions of Fission Gas Release Rates for the SFD-ST Experiment, Compared with the Measured Values and Those Obtained from NUREG-0772.

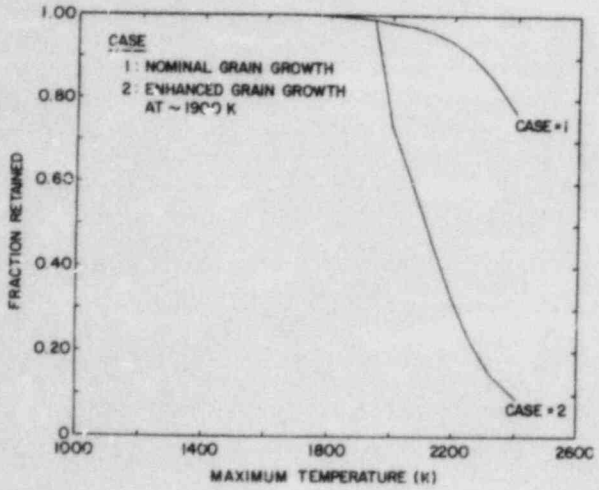

Fig. 1.7.

FASTGRASS-VFP Predictions of Fission Gas Retained Intragranularly at the Hottest Fuel Region during the SFD-ST Experiment, Just Prior to Quench.

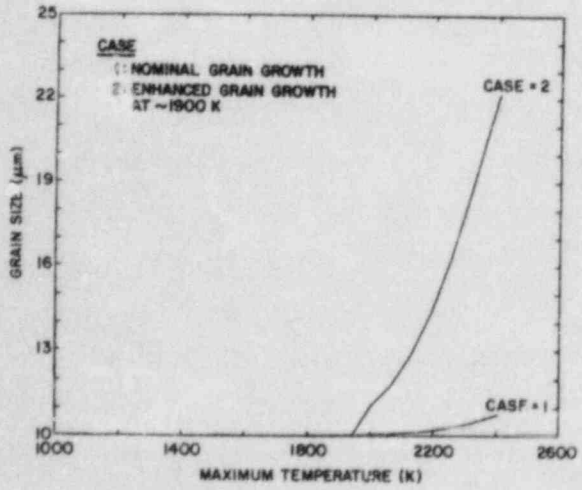

Fig. 1.8.

FASTGRASS-VFP Predictions of Grain Growth in the Hottest Fuel Region during the SFD-ST Experiment.

activation energy is invoked. Since the steam flow conditions of the SFD-ST scoping test produced an oxidizing environment, enhanced grain growth appears appropriate for this analysis. The analysis is also consistent with the fuel-oxidation-enhanced grain growth noted in the PBF-SFD scoping test,[15] where both U_4O_9 precipitates and a substantial increase in grain size were noted upon post-test fuel examination.

In Table 1.1, FASTGRASS-VFP predictions for fission product release during SFD-ST are compared with the measured values. The calculations shown in Table 1.1 were made by assuming that the requench provided the appropriate mechanisms (e.g., fuel fracturing) for the release of the majority of the fission products predicted to be on the grain boundaries. (FASTGRASS-VFP does not currently contain a model for requench-induced processes, e.g., grain boundary fracturing.)

TABLE 1.1 FASTGRASS-VFP Predictions of Fission Product Release During The SFD-ST Test, Compared with the Measured Values

	Fraction Released	
Fission Product	FASTGRASS-VFP Calculation	Collection Tank Measurement
Xe	0.47	~0.50
Cs	0.34	~0.32
I	47	~0.49

The agreement between the theory and the data shown in Table 1.1 is very good. The theory predicts that in the absence of a requench (and fuel liquefaction), very little fission product release would have occurred during SFD-ST. The reason for this result is that owing to the low concentrations of fission gas in this trace-irradiated, low-burnup fuel, very little interconnection of fission gas bubbles is predicted to occur on the grain faces and along the grain edges. This is in contrast to the ORNL transient tests on high-burnup fuel described earlier. The relatively high concentration of fission gas in the high-burnup fuel enables a high degree

of bubble interconnection to occur, with subsequent venting of the retained fission products.

In Fig. 1.9, the measured fission gas release rates for the SFD 1-1 test are compared with the release rates predicted by FASTGRASS-VFP for two values of the maximum fuel temperature. The FASTGRASS-VFP predictions are based on the stoichiometric (nominal) grain growth activation energy for fuel temperatures <1900 K, and on the hyperstoichiometric (enhanced) grain growth activation energy invoked at the time when the peak fuel temperatures exceed >1900 K. A fuel temperature of ~1900 K occurs at ~32-35 minutes into the accident, as is shown in Fig. 1.10. The predicted release rates are seen to increase dramatically upon the initiation of grain-growth-induced sweeping of entrapped intragranular bubbles to grain boundaries. Without such grain-growth-induced sweeping, little gas release is predicted for such low-burnup fuel. It is of particular interest to note that the hyperstoichiometric grain growth activation energy for equiaxed grain growth simulates the test data rather well. Such calculations clearly illustrate the point that for low-burnup fuel, the majority of the fission products remain trapped within the grain interior until elevated temperatures cause sweeping of fission products to grain surfaces and open pores.

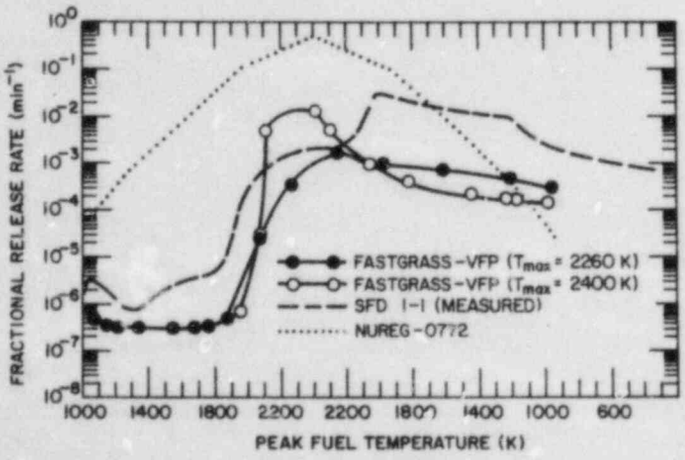

Fig. 1.9. FASTGRASS-VFP Predictions of Fission Gas Release Rates for the SFD 1-1 Experiment, Compared with the Measured Values and Those Obtained from NUREG-0772.

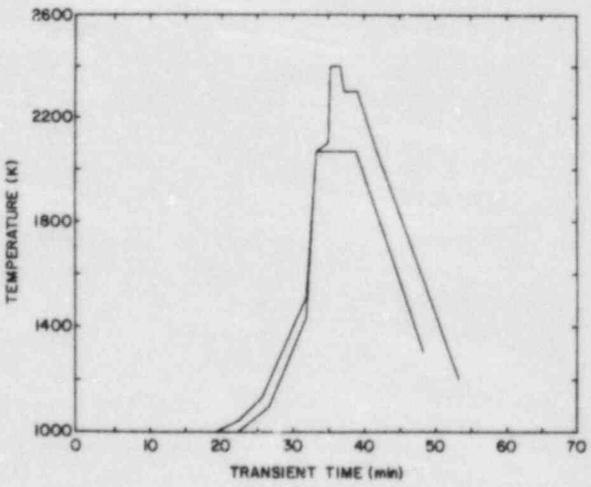

Fig. 1.10. Two Possible Fuel Temperature Scenarios for SFD 1-1 in a Fuel Region ~1/4 L from the Bottom of the Rod, Where L Is Rod Length.

Although the initial release characteristics are modeled fairly well by FASTGRASS-VFP, the total fractional release for the SFD 1-1 test is underpredicted by an order of magnitude (i.e., 2% total predicted release versus ≈20% measured release for the test). This is attributed to the fact that during grain growth, the fission gases are predicted to be swept to grain boundaries, where the majority of such gas is trapped. Owing to the absence of quench-induced grain separation in the SFD 1-1 test, and the fact that FASTGRASS-VFP does not currently model the gas release that accompanies fuel liquefaction,[16] the model predicts gas accumulation at grain surfaces. In actuality the following morphology sequence, leading to fission product release for the SFD 1-1 test, appears probable: (1) initial high gas retention within individual grains due to entrapment of gaseous fission products as individual atoms or intragranular microbubbles, with negligible gas release; (2) grain-growth-induced intragranular microbubble sweeping to grain boundaries at temperatures above ~1900 K, with gas accumulation at grain boundaries and initiation of slow gas release; and (3) destruction of the grain boundary structure by fuel liquefaction (not currently modeled in FASTGRASS-VFP), with attendant rapid gas release.

This suggested sequence of events is supported by the FASTGRASS-VFP prediction of retained intragranular gas in test SFD 1-1 in the absence of fuel liquefaction (for a fuel region ~1/4 L from the bottom of the rod, where L is rod length), shown in Fig. 1.11. The predictions represented by

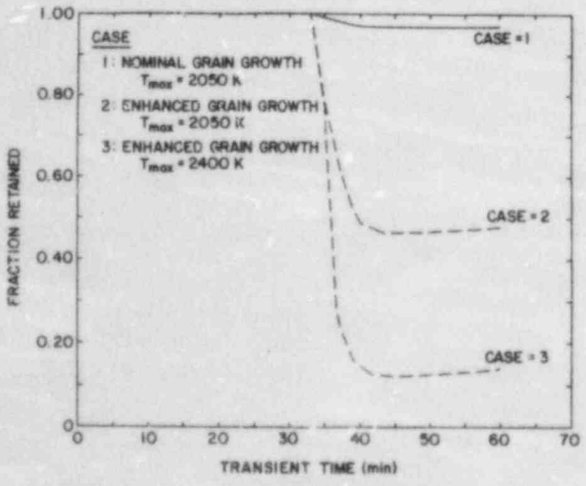

Fig. 1.11. FASTGRASS-VFP Predictions of Fission Gas Retained Intragranularly at a Region ~1/4 L from the Bottom of the Fuel Rod during the SFD 1-1 Experiment, in the Absence of Fuel Liquefaction.

the dotted curves are based on the stoichiometric (nominal) grain growth activation energy, which is invoked for temperatures <1900 K, and the hyperstoichiometric (enhanced) grain growth activation energy, which is invoked when the peak fuel temperature exceeds 1900 K; predictions are given for two values of the maximum fuel temperature (2050 and 2400 K). Also shown in Fig. 1.11 are the predictions of the theory for the case of nominal grain growth with maximum fuel temperature = 2050 K (solid curve). For the situation of fuel-oxidation-enhanced grain growth, a large fraction of the intragranular gas is swept to grain boundaries, with only ~48 and ~12% retention within grains at the end of the transient for the cases where the maximum fuel temperatures are 2050 and 2400 K, respectively.

Figures 1.6 and 1.9 also show fission gas release rates as a function of fuel temperature for the SFD-ST and SFD 1-1 tests, respectively, as calculated from the temperature correlations given in NUREG-0772.[17] As indicated earlier, the FASTGRASS-VFP-predicted and measured release rates agree quite well; however, these rates are about 4 orders of magnitude lower than the predicted rates based upon the NUREG-0772 temperature correlations. This discrepancy is due, in part, to the fission product morphology characteristics of the trace-irradiated fuel employed in the SFD-ST and SFD 1-1 tests. The NUREG-0772 correlations were developed primarily from release experience for medium- to high-burnup fuel under relatively isothermal test conditions; in contrast, the SFD-ST and SFD 1-1 tests were non-isothermal, and the fuel used in these tests was essentially fresh (except for the development of a small inventory of fission products at an effective burnup level of approximately 0.0089 atom-percent). FASTGRASS-VFP analyses indicate that for trace-irradiated fuel, the vast majority of both fission gases and volatiles (I and Cs) are still retained within the interior of individual grains either as individual atoms or as newly nucleated intragranular microbubbles. FASTGRASS-VFP calculations indicate that such morphology will exist until grain growth causes the sweeping of intragranular microbubbles to grain boundaries. Since grain growth normally requires fuel temperatures in excess of 1900 K, significant release during the heatup phase of these PBF/SFD tests is precluded. Only when temperatures above 1900 K cause destruction of the grain boundary

structure (by eutectic fuel melting and/or quench-induced processes such as grain boundary fracturing) is significant release predicted for such low-burnup fuel.

The effect of burnup on fission product release and grain growth is further demonstrated in Figs. 1.12 and 1.13, respectively, which show FASTGRASS-VFP predictions for SFD 1-1 accident conditions as a function of as-irradiated burnup. Fission gas release during the accident is predicted to increase dramatically as the as irradiated burnup is increased from 0.01 to ~3 at.% (see Fig. 1.12). However, above ~3 at.% burnup, the predicted fission gas release decreases and tends to saturate at a relatively constant value. The reason for the dramatic increase in gas release for burnups between 0.01 and 3 at.% is that the higher burnup fuel has an increased development of fission gas bubbles on the grain boundaries, which provide an increased degree of interconnection to a free surface. At burnups >3 at.%, however, the fission gas release is limited by a substantial decrease in the grain boundary sweeping of intragranular gas to the grain surface; this is due to a decrease in the predicted grain growth, which is a consequence of the increased development of fission gas bubbles on the grain boundaries (see Fig. 1.13).

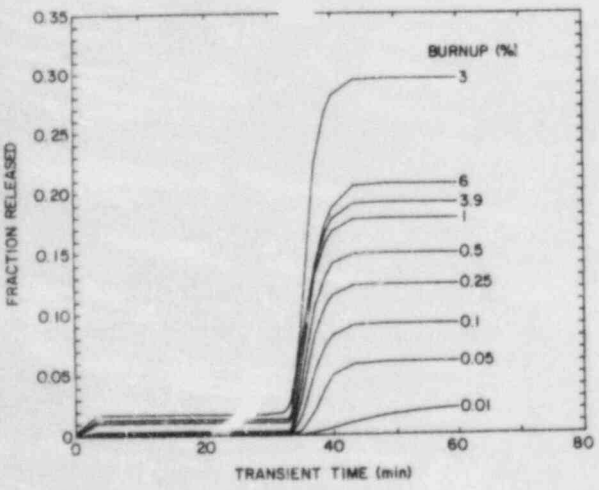

Fig. 1.12. FASTGRASS-VFP Predictions of Fission Gas Release for the SFD 1-1 Experiment as a Function of Fuel Burnup.

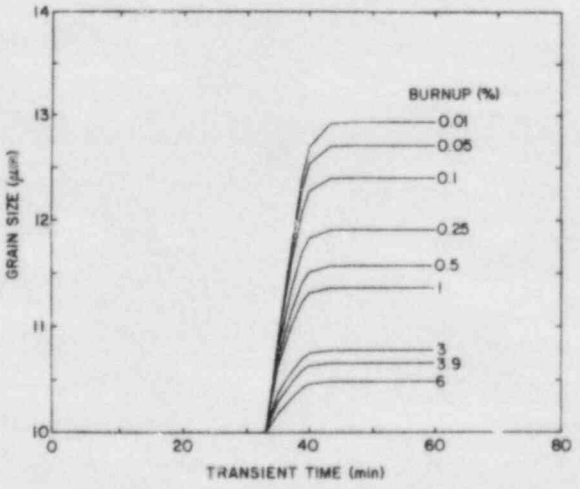

Fig. 1.13. FASTGRASS-VFP Predictions of Grain Growth for the SFD 1-1 Experiment as a Function of Fuel Burnup.

A conclusion that can be drawn from the above analyses is that rapid fission gas release processes such as liquefaction and those induced by a requench, although very important at low burnup (<0.5 at.%), will not have as significant an effect on the release of fission products at high burnup (>0.5 at.%).

D. Conclusions

The results of the FASTGRASS-VFP analysis indicate that for the SFD-ST and SFD 1-1 tests, the sequence of events leading to fission product release appears to be as follows: (1) initial high fission product retention within individual grains due to entrapment of fission products as individual atoms or intragranular microbubbles, with negligible release; (2) grain-growth-induced intragranular atomic and microbubble sweeping to grain boundaries at temperatures in excess of 1900 K, with attendant bubble growth and gas accumulation at the grain boundaries and initiation of slow gas and VFP release; (3) destruction of the grain boundary structure via fuel liquefaction and/or quench-induced processes (e.g., grain-boundary fracturing), with attendant rapid intergranular gas release.

FASTGRASS-VFP theory correctly predicts the fission product behavior of high-burnup fuel during the ORNL high-temperature heating tests. The results of the analysis indicate that a grain-growth/grain-boundary-sweeping mechanism is responsible for the relatively large intragranular fission product release predicted to occur during the majority of these tests. FASTGRASS-VFP-predicted grain sizes for tests HI-1, HI-2, HI-3, and HI-4 are in reasonable agreement with grain growth observations made on the tested fuel. The measured grain growth for the high-burnup fuel used in these ORNL high-temperature heating tests is substantially less than the observed grain growth for the PBF tests on trace-irradiated fuel. These results are interpreted in the context of the theory for grain-growth/grain-boundary-sweeping in that the accumulation of fission products on the grain boundaries of high-burnup fuel retards grain boundary movement.

The results of FASTGRASS-VFP Analyses indicate the inappropriateness of extrapolating the NUREG-0772 correlations, which are based primarily upon

medium-to high-burnup data, to determine release characteristics for the trace-irradiated fuel employed in the PBF tests. This is because at extremely low burnup, there does not exist a sufficient inventory of fission gases to precipitate the development of a network of interconnected porosity necessary for gas release from the fuel interior to the pellet surface. Only upon initiation of enhanced grain growth at elevated temperatures (>1900 K), and destruction of the grain boundary structure by liquefaction and/or quench-induced processes, would significant release be expected for these low-burnup conditions.

E. References for Chapter I

1. J. Rest, in Proc. Int. Mtg. Thermal Nuclear Reactor Safety, Chicago, IL, August 29-September 2, 1982, NUREG/CP-0027, Vol. 1 (February 1983), pp. 111-121.

2. J. Rest, Nucl. Technol. 61, 33-48 (1983).

3. J. Rest, J. Nucl. Mater. (in press, 1984).

4. S. W. Tam, P. E. Blackburn, and C. E. Johnson, in Proc. Int. Mtg. Thermal Nuclear Reactor Safety, Chicago, IL, August 29-September 2, 1982, NUREG/CP-0027, Vol. 1 (February 1983), pp. 101-110.

5. J. Rest, in Proc. Top. Mtg. Fission Product Behavior and Source Term Research, Snowbird, Utah, July 15-19, 1984 (in press, 1984).

6. D. R. Olander, Fundamental Aspects of Nuclear Reactor Fuel Elements, U. S. Energy Research and Development Administration, Washington, DC (1976).

7. M. V. Speight and G. W. Greenwood, Philos. Mag., 9, 683 (1964).

8. J. Belle, Uranium Dioxide, U. S. Government Printing Office, Washington, DC, (1961), pp. 512-515.

9. J. R. Macewan and J. Hayashi, Proc. Brit. Ceram. Soc. 7, 245 (1967).

10. J. A. Turnbull, A Review of Rare Gas Diffusion in Uranium Dioxide, unpublished work, 1972.

11. M. F. Osborne et al., in Proc. Top. Mtg. Fission Product Behavior and Source Term Research, Snowbird, Utah, July 15-19, 1984 (in press, 1984).

12. R. V. Strain, ibid.

13. Hj. Matzke, J. Nucl. Mater. 25, 209-221 (1967).

14. R. M. Cornell, Philos. Mag. 19, 539 (1969).

15. D. J. Osetek, R. R. Hobbins, K. Vinjamuri, and A. W. Cronenberg, in Proc. Top. Mtg. Fission Product Behavior and Source Term Research, Snowbird, Utah, July 15-19, 1984 (in press, 1984).

16. A. W. Cronenberg et al., in Proc. Int. Mtg. Light Water Reactor Severe Accident Evaluation, Cambridge, Mass., August 28-September 1, 1983 (American Nuclear Society, LaGrange Park, IL, 1983) Vol. I, pp. 4.5-1 to 4.5-8.

17. U. S. Nuclear Regulatory Commission, Technical Basis for Estimating Fission Product Behavior During LWR Accidents, NUREG-0772 (June 1981).

II. CLAD PROPERTIES FOR CODE VERIFICATION

Principal Investigators:
H. M. Chung, F. L. Yaggee, and T. F. Kassner

The Zircaloy cladding of fuel rods in light-water-cooled reactors is susceptible to local breach-type failures, commonly known as pellet-cladding interaction (PCI) failures, during power transients after the fuel has achieved sufficiently high burnup. As a result of the high burnup, the gap between the UO_2 fuel pellets and the cladding is closed and highly localized stress is believed to be imposed on the cladding by differential thermal expansion of the cracked fuel and cladding during power transients. In addition to the localized stress, a high-burnup fuel cladding is also characterized by high-density radiation-induced defects (RID), mechanical constraints imposed by pellet-cladding friction, compositional changes (e.g., oxygen and hydrogen uptake associated with in-service corrosion), and geometrical changes due to creep-down and bowing. It is possible that synergistic effects involving more than one of the above factors influence the deformation and fracture of the in-reactor fuel cladding, e.g., strain aging associated with impurity or alloying elements, irradiation- or stress-induced segregation of the elements and subsequent formation of non-equilibrium phases. Although mechanisms of stress corrosion cracking (SCC) associated with volatile fission products such as I and liquid metal embrittlement (LME) associated with an element such as Cd have been well established for local breach-type failures of irradiated and unirradiated Zircaloy cladding under out-of-reactor simulation conditions, conclusive evidence of these processes is not yet available for in-reactor PCI failures. Consequently, to provide a better understanding of the PCI phenomenon, we have undertaken a mechanistic study of the deformation and fracture behavior of actual power-reactor fuel cladding discharged after a high burnup.

In this program, the effect of temperature, strain rate, and stress localization on the deformation and fracture characteristics of Zircaloy cladding from spent-fuel rods is being investigated by means of internal gas-pressurization and mandrel-loading experiments in the absence of simulated fission product species. The deformed and fractured specimens of spent-fuel

cladding are then being examined by optical microscopy, scanning electron microscopy (SEM), transmission electron microscopy (TEM), and high-voltage electron microscopy (HVEM). The results of microstructural and fracture-property investigations will be used to develop a failure criterion for the cladding under PCI-type loading conditions. The information will be incorporated into fuel performance codes, which can be used to evaluate the susceptibility of extended-burnup fuel elements in commercial reactors to PCI failures during power transients in later cycles, and to evaluate cladding performance and reliability of new fuel-element designs. An optimization of power ramp procedures to minimize cladding failures would result in a significant decrease in radiation exposure of plant personnel due to background and airborne radioactivity as well as an extension of core life in terms of allowable off-gas radioactivity.

A. Observation of Zr_3O Precipitates on Dislocation Substructures (H. M. Chung)

1. Introduction

It has been reported previously that spent-fuel cladding specimens that failed in a PCI-like brittle manner were characterized by small failure strains, a large extent of pseudocleavage plus fluting in the fracture surface, and a very low dislocation density.[1] It was also shown that the Zr_3O phase was observed primarily in association with dislocation substructures of a specimen that failed in a brittle manner.[1] Dark-field morphologies obtained from the Zr_3O superlattice reflections showed that the dislocations were decorated by small Zr_3O precipitates.[2] In this reporting period, a large number of diffraction patterns, which were obtained from the dislocation substructures of brittle-type failure specimens, were analyzed for the superlattice reflections. As a result, the fraction of the number of diffraction patterns that contained the superlattice reflections were determined out of a total of ~40 patterns. The fraction, designated as an s-parameter, is an indication of the extent of the Zr_3O phase precipitation on and immobilization of the dislocations. The parameter is useful, in that it can be correlated quantitatively

with the fracture characteristics of the specimen, e.g., the F_p-parameter which defines the extent of penetration of pseudocleavage plus fluting on the fracture surface.[1]

2. s-parameter of the Big Rock Point Cladding Specimen 165AE4B

The Big Rock Point cladding tube 165AE4B failed at 325°C in a brittle-type manner during internal gas-pressurization loading. The pseudocleavage plus fluting failure, characteristic of a pellet-cladding-interaction failure, penetrated up to 78% of the wall thickness at the failure site, i.e., $F_p = 0.78$.[1] TEM-HVEM examination of a thin-foil specimen (adjacent to the failure site) revealed a very small density of dislocations compared to other specimens that failed in a ductile manner (i.e., specimens with $F_p = 0$).[1] Selected-area diffraction patterns of the area containing the dislocation substructures of the specimen usually showed the Zr_3O superlattice reflections. A few typical examples are shown in Figs. 2.1 and 2.2, which were obtained from 1-MeV HVEM and 100-keV TEM, respectively. Numerous superlattice reflections are shown in the indexed diffraction patterns of Figs. 2.1(C) and 2.2(B). From the dark-field images of Figs. 2.1(D) and 2.2(C) and (D), it can be observed that the individual dislocations are decorated by small Zr_3O particles of the order of 10 nm (100 Å) or less in size.

The results of diffraction analyses for the presence of Zr_3O superlattice reflections, similar to those of Figs. 2.1 and 2.2, are summarized in Table 2.1. Overall, the results in Table 2.1 indicate the extent of Zr_3O precipitation on the dislocation substructures and the immobilization of the dislocations in the specimen. Out of a total of 39 selected-area diffraction patterns analyzed, 24 contained superlattice reflections. This corresponds to 61.5%, i.e., an s-parameter of 0.615, for the 165AE4B specimen.

A preliminary result from a similar analysis of the 165AE4A specimen, which failed in a ductile manner (i.e., $F_p = 0$),[1] yielded an s-parameter of ~0.097. Detailed results for the specimen will be reported in the next reporting period.

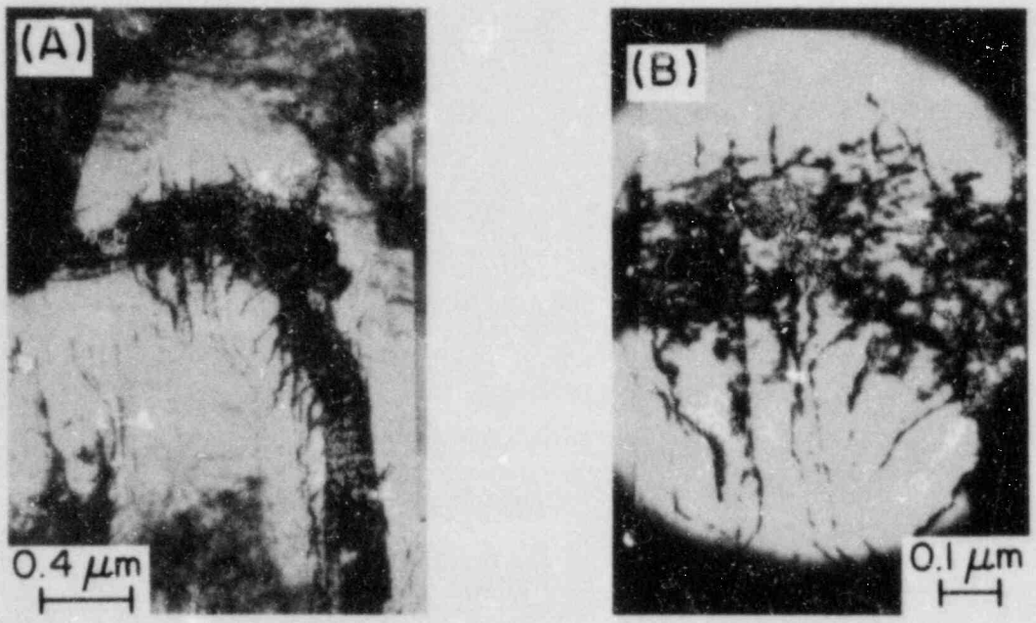

Fig. 2.1. 1-MeV HVEM Micrographs Obtained from the Big Rock Point Cladding Tube 165AE4B That Failed in a PCI-like Brittle Manner. (A) Bright-field image containing dislocation substructure, (B) higher magnification of a selected area of (A), (C) indexed diffraction pattern of (B) showing Zr_3O superlattice reflections, (D) dark-field image (negative contrast) of the circled spot of (C).

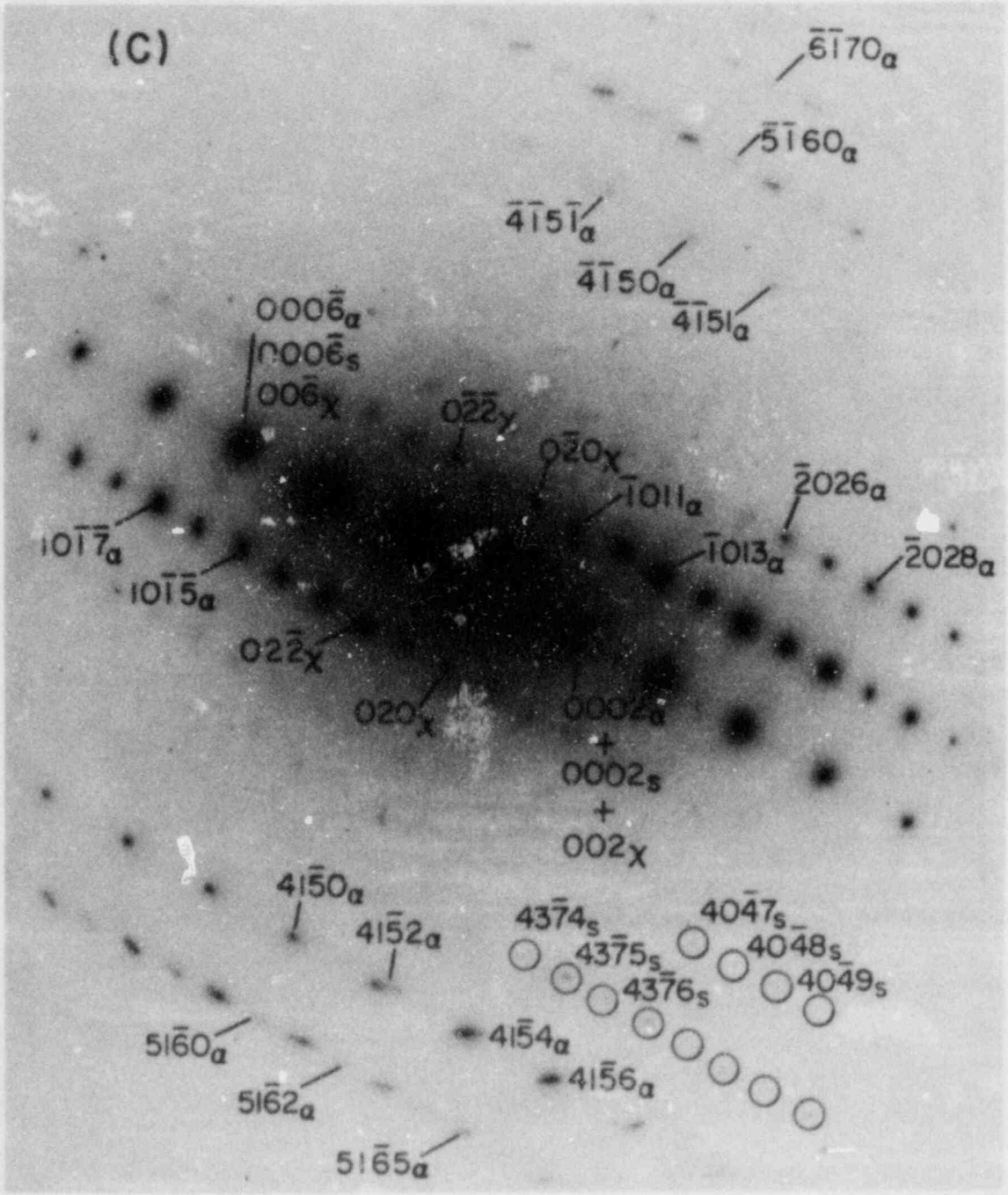
(C)
$\bar{5}\bar{1}70_\alpha$
$\bar{5}\bar{1}60_\alpha$
$\bar{4}\bar{1}5\bar{1}_\alpha$
$\bar{4}\bar{1}50_\alpha$
$\bar{4}\bar{1}5\bar{1}_\alpha$
0006_α
0006_s
006_χ
$02\bar{2}_\chi$
$0\bar{2}0_\chi$
$\bar{1}011_\alpha$
$\bar{2}026_\alpha$
$10\bar{1}\bar{7}_\alpha$
$\bar{1}013_\alpha$
$\bar{2}028_\alpha$
$10\bar{1}\bar{5}_\alpha$
$02\bar{2}_\chi$
020_χ
0002_α
+
0002_s
+
002_χ
$41\bar{5}0_\alpha$
$43\bar{7}4_s$
$40\bar{4}7_s$
$41\bar{5}2_\alpha$
$43\bar{7}5_s$
$40\bar{4}8_s$
$43\bar{7}6_s$
$40\bar{4}9_s$
$51\bar{6}0_\alpha$
$41\bar{5}4_\alpha$
$41\bar{5}6_\alpha$
$51\bar{6}2_\alpha$
$51\bar{6}5_\alpha$

Fig. 2.1. (Contd.)

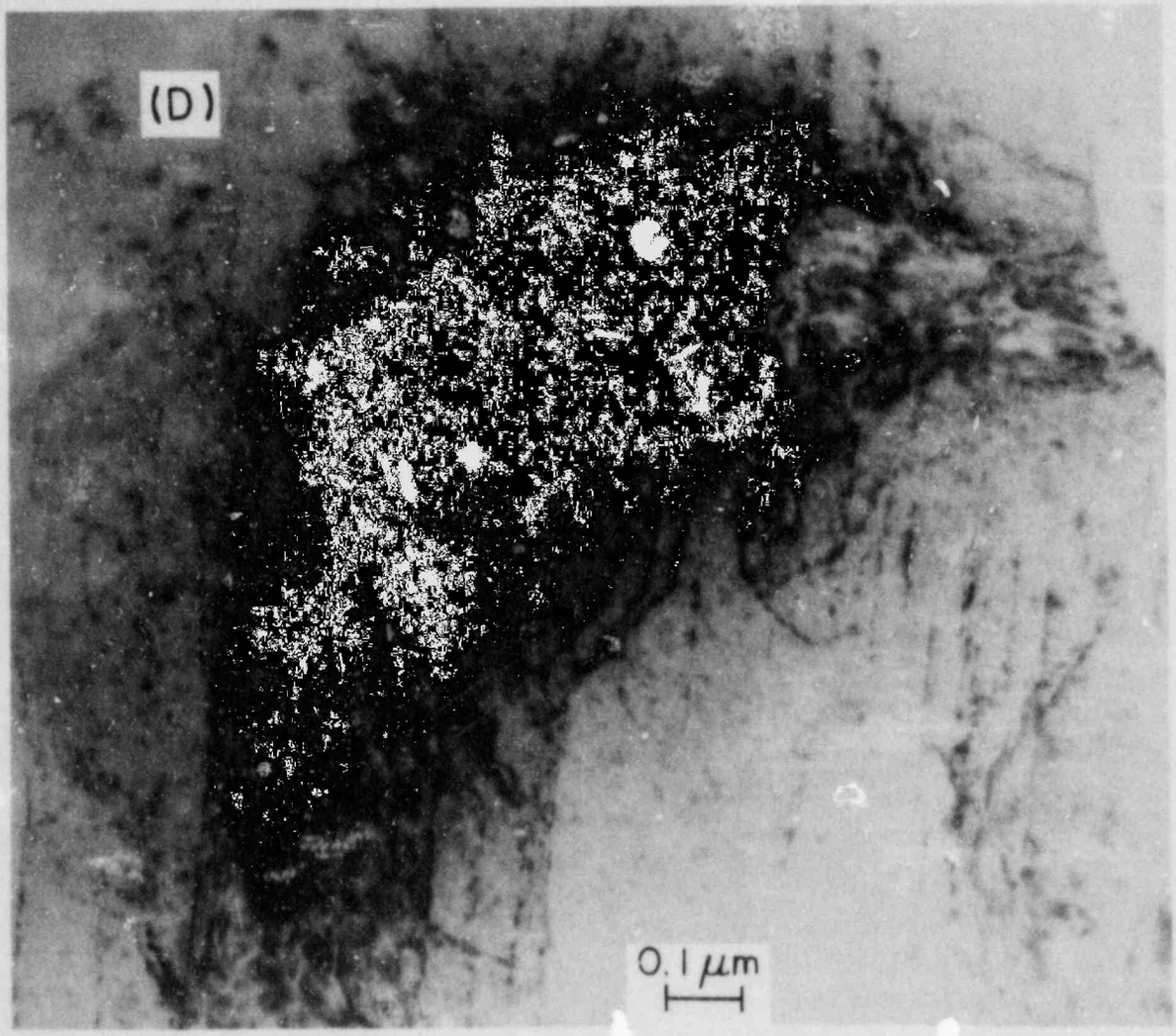

Fig. 2.1. (Contd.)

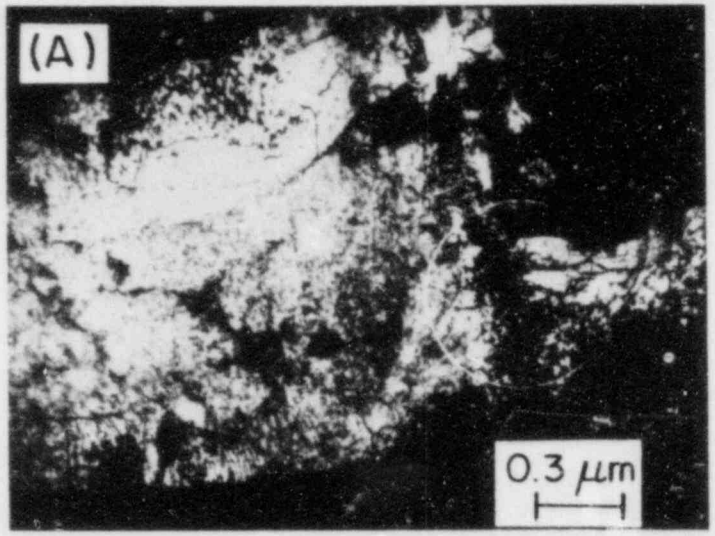

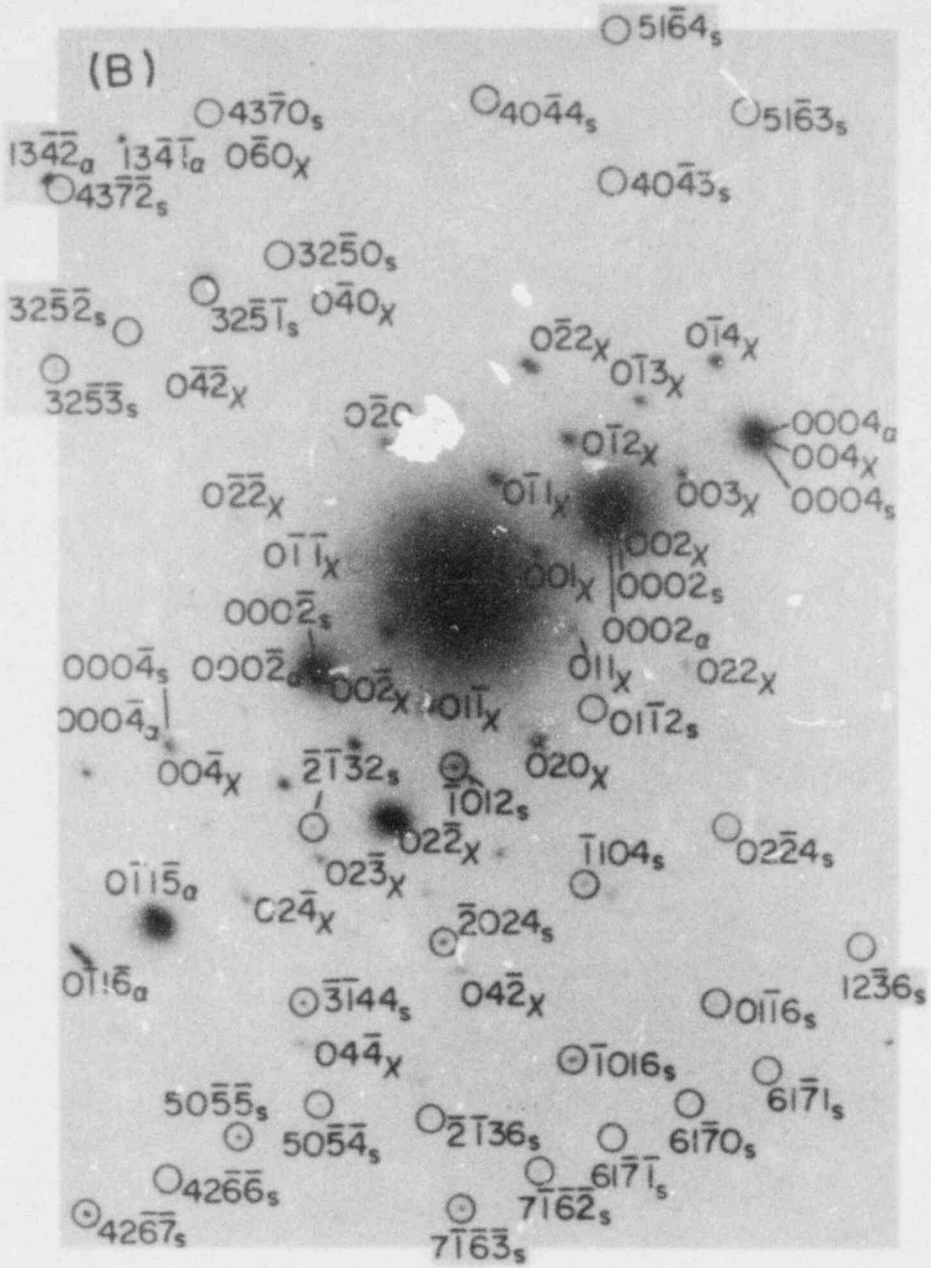

Fig. 2.2.

100-keV TEM Micrographs Obtained from the Big Rock Point Cladding Tube 165AE4B That Failed in a PCI-like Brittle Manner. (A) Bright-field image containing dislocation substructure, (B) indexed diffraction pattern of the circled selected area of (A) showing Zr_3O superlattice reflections, (C) dark-field image (negative contrast) of the circled spot of (B), and (D) higher magnification of (C).

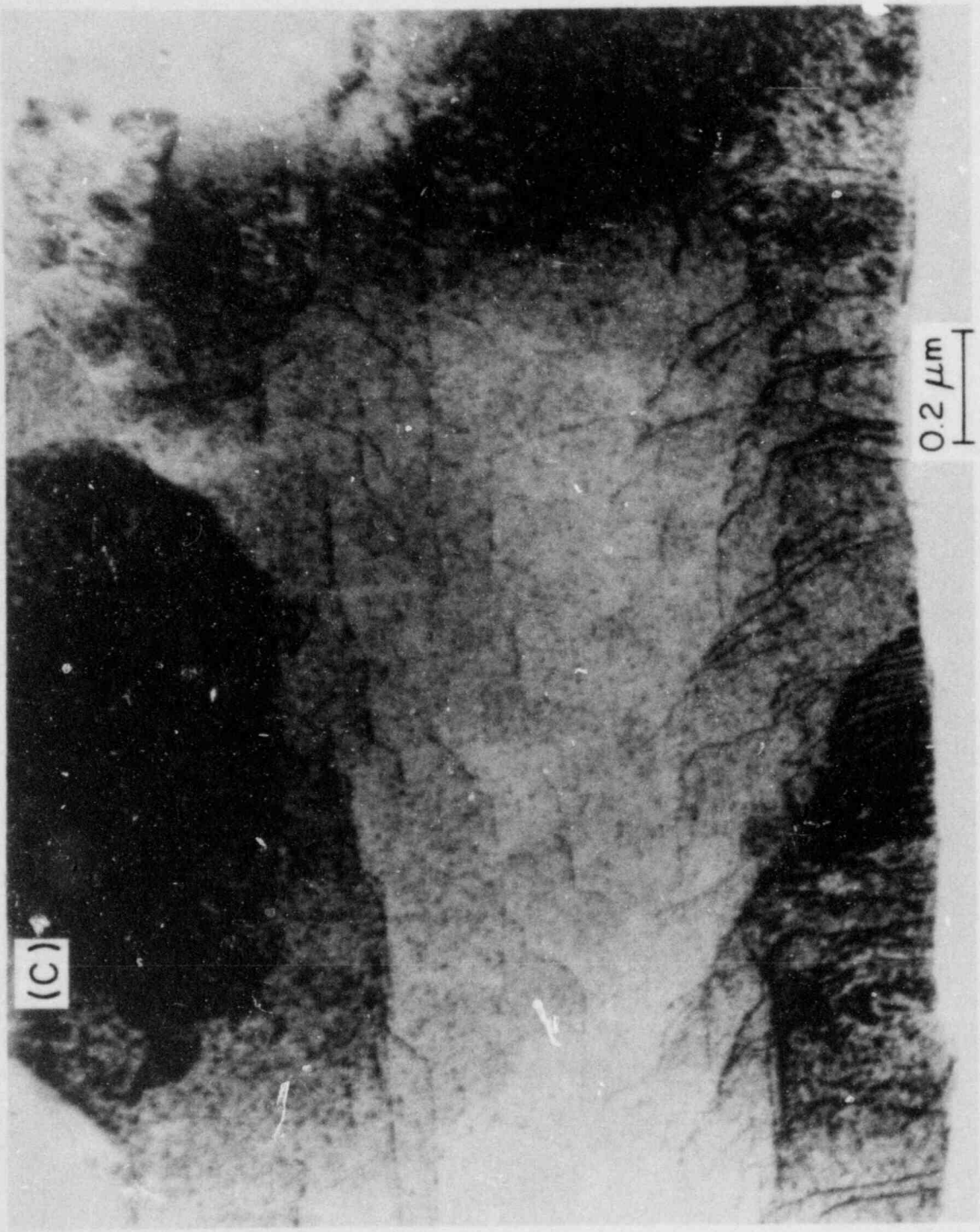

Fig. 2.2. (Contd.)

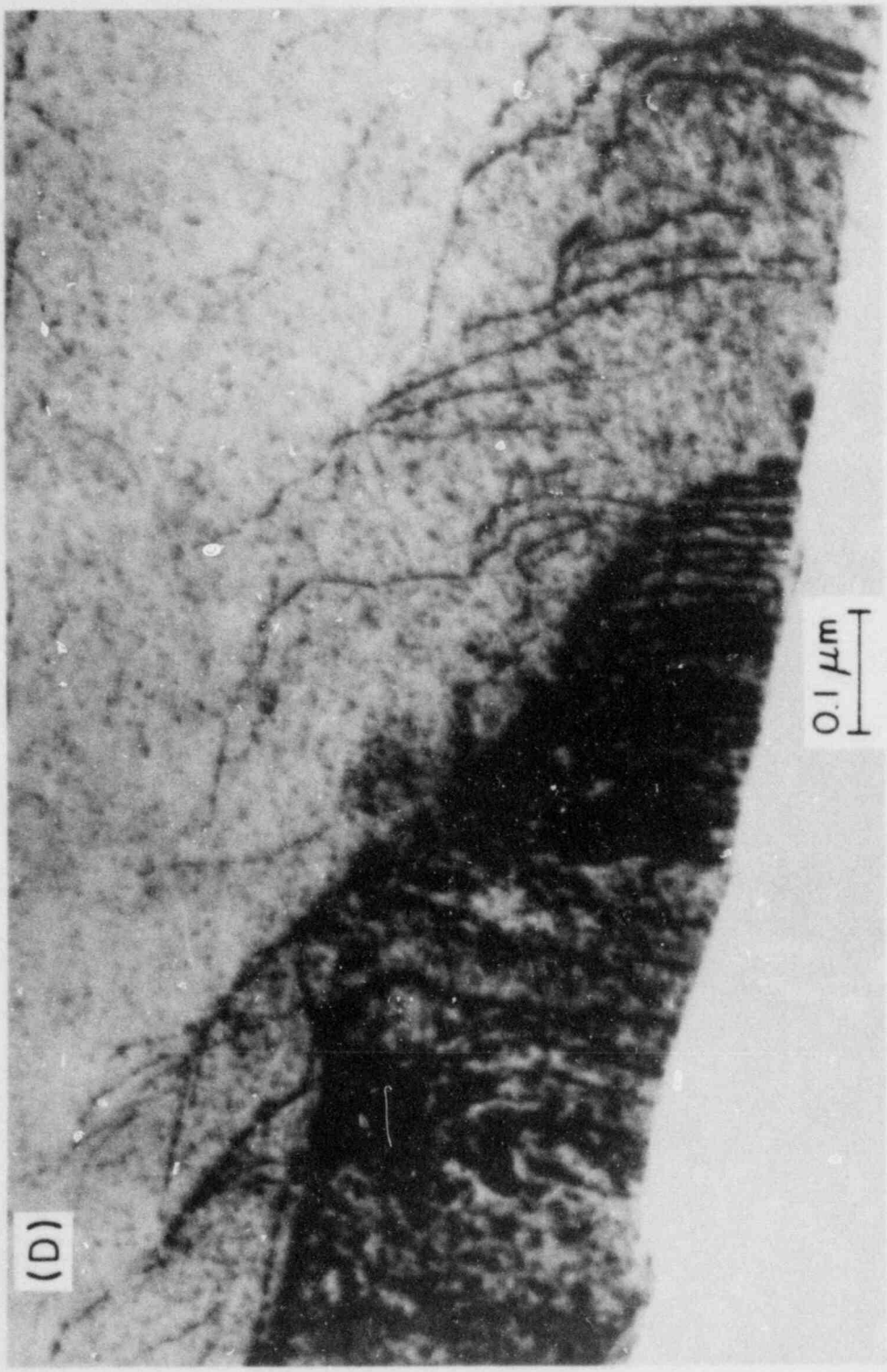

Fig. 2.2. (Contd.)

TABLE 2.1. Summary of TEM-HVEM Analyses of Zr_3O Superlattice Reflections Observed in Association with Dislocation Substructures in the Big Rock Point Spent-Fuel Cladding Specimen 165AE4B Which Failed in a Brittle Manner at 325°C by Internal Gas Pressurization[a]

Identification No. of Selected-Area Diffraction Pattern	Identification No. of Selected-Area Bright-Field Image[b]	Observed Zr_3O Superlattice Reflections[c]	Dark-Field Image Available
34350	34348	$\bar{5}\bar{5}4$, $\bar{5}\bar{5}5$, $\bar{7}\bar{2}2$, $\bar{7}\bar{2}3$, $\bar{8}\bar{1}4$, $\bar{8}\bar{1}3$, $\bar{8}\bar{1}2$	002
34132	34131	$80\bar{2}$, $80\bar{3}$, $80\bar{4}$, $80\bar{5}$, $80\bar{6}$	$00\bar{2}$
8606	8605	None	
34137	34136	324, 325, 326, 327	$00\bar{2}$
34141	34130	$80\bar{2}$, $80\bar{3}$, $80\bar{4}$, $80\bar{5}$	
34143	34142	$80\bar{2}$, $80\bar{3}$, $80\bar{4}$ $\bar{4}\bar{2}\bar{5}$, $\bar{4}\bar{2}\bar{6}$, $\bar{4}\bar{2}\bar{7}$, $\bar{4}\bar{2}\bar{8}$	
34145	34144	$32\bar{4}$, $32\bar{5}$, $32\bar{6}$, $32\bar{7}$	
34583	34582	$\bar{5}\bar{4}0$, $\bar{5}\bar{4}\bar{1}$, $54\bar{2}$, $31\bar{2}$, $31\bar{3}$, 310, 311, 312, 313	$00\bar{2}$
35275	35273	420, $42\bar{1}$, $42\bar{2}$, $42\bar{3}$, $42\bar{4}$	002

TABLE 2.1. (Contd.)

Identification No. of Selected-Area Diffraction Pattern	Identification No. of Selected-Area Bright-Field Image[b]	Observed Zr_3O Superlattice Reflections[c]	Dark-Field Image Available
34579	34577	430, 43$\bar{1}$, 43$\bar{2}$, 320, 32$\bar{1}$, 32$\bar{2}$, 32$\bar{3}$, 404, 403, 514, 513, 012, $\bar{1}$02, $\bar{2}\bar{1}$2, 024, $\bar{1}$14, $\bar{2}$04, $\bar{3}\bar{1}$4, 50$\bar{4}$, 50$\bar{5}$, 42$\bar{6}$, 42$\bar{7}$, $\bar{2}\bar{1}$6, $\bar{1}$06, 016, 126, 7$\bar{1}\bar{3}$, 7$\bar{1}\bar{2}$, 61$\bar{1}$, 610 611	002
33312	33310	None	00$\bar{2}$
34296	34294	626, 627, 424, 425, 426, 427, 315, 316, 317	002, $\bar{2}$15
6089	6087	None	002
34587	--	430, 43$\bar{1}$, 43$\bar{2}$, $\bar{3}\bar{2}\bar{1}$, $\bar{3}\bar{2}\bar{2}$, $\bar{3}\bar{2}\bar{3}$,	
34285	34284	832, 831, 830	00$\bar{2}$
34590	34589	None	002
35290	35289	43$\bar{2}$, 43$\bar{1}$, 430, 431, 432	
35292	35291	None	

TABLE 2.1. (Contd.)

Identification No. of Selected-Area Diffraction Pattern	Identification No. of Selected-Area Bright-Field Image[b]	Observed Zr_3O Superlattice Reflections[c]	Dark-Field Image Available
35294	35293	None	
35298	35297	None	
35300	35299	800, 80$\bar{1}$, 80$\bar{2}$	
35302	35301	42$\bar{4}$, 42$\bar{3}$, 42$\bar{2}$, 42$\bar{1}$, 420, 421, 422, 423, 424, 425	
35305	35304	43$\bar{2}$, 43$\bar{1}$, 430, 431, 432, 433, 311, 312, 313, 314, 315, 316	
35307	35306	72$\bar{2}$, 72$\bar{3}$, 72$\bar{4}$, 801, 800, 80$\bar{1}$, 80$\bar{2}$	
35309	35308	None	
8593	8590	0$\bar{1}$7, 0$\bar{1}$8, 0$\bar{1}$9, 0$\bar{1}$10, 0$\bar{1}$11, 019, 0110, 0111	002

TABLE 2.1. (Contd.)

Identification No. of Selected-Area Diffraction Pattern	Identification No. of Selected-Area Bright-Field Image[b]	Observed Zr_3O Superlattice Reflections[c]	Dark-Field Image Available
34975	34964	$\bar{6}\bar{2}1$, $\bar{6}\bar{2}2$, $\bar{6}\bar{2}3$,	$00\bar{2}$
		$\bar{6}\bar{2}4$, $\bar{4}\bar{2}1$, $\bar{4}\bar{2}2$,	
		$\bar{4}\bar{2}3$, $\bar{5}\bar{1}4$, $\bar{5}\bar{1}5$,	
		$\bar{5}\bar{1}6$, $\bar{3}\bar{1}5$, $\bar{3}\bar{1}6$,	
		612, 613	
34358	34361	433, 434, 435	
34587	-	$43\bar{2}$, $43\bar{1}$, 430,	
		$32\bar{3}$, $32\bar{2}$, $32\bar{1}$	
34589	34586	None	
27172	27174	None	
8039	8038	None	
8049	8047	407, 408, 409,	$00\bar{2}$
		4010, 4011, 435,	
		436, 437, 438,	
		439, 4310, 4311,	
		4312, 4313, $31\bar{7}$,	
		$31\bar{8}$, $31\bar{9}$, $\bar{3}\bar{1}5$,	
		$\bar{3}\bar{1}6$, $\bar{3}\bar{1}7$, $\bar{3}\bar{1}8$,	
		$\bar{3}\bar{1}9$	

[a]For information on burnup, fluence, mechanical test conditions, SEM fractographic, and metallographic characteristics, see Ref. 1.
[b]Bright-field image of the selected area containing the dislocation substructures.
[c]Denoted in Miller indices.

B. References for Chapter II

1. H. M. Chung, "TEM-HVEM Observation of Ordered Zirconium-Oxygen Phase in Zircaloy Spent-Fuel Cladding," in Proc. Intl. Symp. on Environmental Degradation of Materials in Nuclear Power Systems-Water Reactors, Myrtle Beach, SC, August 22-24, 1983 (in press).

2. H. M. Chung, in Materials Science and Technology Division Light-Water-Reactor Safety Research Program: Quarterly Progress Report, October-December 1983, NUREG/CR-3689 Vol. IV, ANL-83-85 Vol. IV, pp. .

Distribution for NUREG/CR-3980 Vol. I (ANL-84-61 Vol. I)

Internal:

R. Avery
O. K. Chopra
H. M. Chung
L. W. Deitrich
C. E. Dickerman
D. R. Diercks
G. R. Fenske
F. Y. Fradin
B. R. T. Frost
E. E. Gruber
G. L. Hofman
M. Ishii
W. D. Jackson
C. E. Johnson
T. F. Kassner (10)
K. L. Kliewer
J. M. Kramer
D. S. Kupperman
D. J. Lam
Y. Y. Liu
P. A. Lottes
P. S. Maiya
D. K. Moores
K. Natesan
L. A. Neimark
F. A. Nichols
P. R. Okamoto
R. G. Palm
J. Y. Park
R. B. Poeppel
L. E. Rehn
J. Rest (10)
W. E. Ruther
R. A. Scharping
W. J. Shack (3)
E. M. Stefanski (2)
R. V. Strain
C. E. Till
H. C. Tsai
R. A. Valentin
A. Villalobos
R. W. Weeks
H. Wiedersich
F. L. Yaggee
ANL Patent Dept.
ANL Contract File
ANL Libraries (3)
TIS Files (6)

External:

NRC, for distribution per R3 (275)
DOE-TIC (2)
Manager, Chicago Operations Office, DOE
R. Tom, DOE-CH
Materials Science and Technology Division Review Committee:
B. Alcock, U. Toronto
A. Arrott, Simon Fraser U.
R. C. Dynes, Bell Labs., Murray Hill
A. G. Evans, U. California, Berkeley
H. K. Forsen, Bechtel Group, San Francisco
E. Kay, IBM San Jose Research Lab.
B. Maple, U. California, San Diego
P. G. Shewmon, Ohio State U.
J. K. Tien, Columbia U.
J. W. Wilkins, Cornell U.
R. B. Adamson, General Electric Co., Vallecitos Nuclear Center, P. O. Box 460, Pleasanton, Calif. 94566
P. L. Andresen, General Electric Corporate Research and Development, Schenectady, N. Y. 12301
G. A. Arlotto, Office of Nuclear Regulatory Research, USNRC, Washington
D. Atteridge, Battelle Pacific Northwest Lab., P. O. Box 999, Richland, Wash. 99352
D. L. Burman, Westinghouse PWR Systems Div., P. O. Box 355, Pittsburgh, Pa. 15230
L. K. Chan, Office of Nuclear Regulatory Research, USNRC, Washington
B. Cox, Chalk River Nuclear Labs., AECL, Chalk River, Ont., K0J 1J0, Canada
R. B. Foulds, Office of Nuclear Reactor Regulation, USNRC, Washington
S. M. Gehl, Electric Power Research Inst., P. O. Box 10412, Palo Alto, Calif. 94304
J. H. Gittus, Springfields Nuclear Power Development Labs., U. K. Atomic Energy Authority, Springfields, Salwick, Preston, PR4 ORR, England
R. R. Hobbins, EG&G/INEL, 1520 Sawtelle Dr., Idaho Falls, Idaho 83401
W. V. Johnston, Office of Nuclear Reactor Regulation, USNRC, Washington

R. L. Jones, Electric Power Research Inst., P. O. Box 10412, Palo Alto, Calif. 94304
K. R. Jordan, Nuclear Fuel Div., Monroeville Nuclear Center, Westinghouse Electric Corp., Monroeville, Pa. 15146
C. N. Kelber, Office of Nuclear Regulatory Research, USNRC, Washington
E. Kohn, Atomic Energy of Canada Ltd., Sheridan Park Research Community, Mississauga, Ont., Canada L5K 1B2
P. M. Lang, Office of Converter Reactor Deployment, USDOE, Washington, D. C. 20545
D. D. Lanning, Battelle Pacific Northwest Lab., P. O. Box 999, Richland, Wash. 99352
R. A. Lorenz, Oak Ridge National Lab., P. O. Box X, Oak Ridge, Tenn. 37830
P. MacDonald, EG&G/INEL, 1520 Sawtelle Dr., Idaho Falls, Idaho 83401
G. P. Marino, Office of Nuclear Regulatory Research, USNRC, Washington
S. McDonald, Westinghouse Electric Corp., R&D Center, Beulah Rd., Pittsburgh, Pa. 15235
K. R. Merckx, Exxon Nuclear, Inc., 2955 George Washington Way, Richland, Wash. 99352
A. C. Millunzi, Office of Breeder Reactor Programs, USDOE, Washington D. C. 20545
D. R. O'Boyle, Commonwealth Edison Co., P. O. Box 767, Chicago, Ill. 60690
R. N. Oehlberg, Electric Power Research Inst., P. O. Box 10412, Palo Alto, Calif. 94304
M. F. Osborne, Oak Ridge National Lab., P. O. Box X, Oak Ridge, Tenn. 37830
D. E. Owen, EG&G Idaho, P. O. Box 88, Middletown, Pa. 17057
T. P. Papazoglou, Lynchburg Research Center, Babcock & Wilcox Co., P. O. Box 1260, Lynchburg, Va. 24505
J. T. A. Roberts, Electric Power Research Inst., P. O. Box 10412, Palo Alto, Calif. 94304
H. H. Scott, Office of Nuclear Regulatory Research, USNRC, Washington
R. D. Silver, Office of Nuclear Reactor Regulation, USNRC, Washington
P. Smerd, Combustion Engineering, Inc., P. O. Box 500, Windsor, Conn. 06095
A. A. Solomon, School of Nuclear Engineering, Purdue U., West Lafayette, Ind. 47907
R. Van Houten, Office of Nuclear Regulatory Research, USNRC, Washington

NRC FORM 335 (2-84) NRCM 1102, 3201, 3202

U.S. NUCLEAR REGULATORY COMMISSION

BIBLIOGRAPHIC DATA SHEET

SEE INSTRUCTIONS ON THE REVERSE

1. REPORT NUMBER (Assigned by TIDC, add Vol. No., if any)
NUREG/CR-3980 Vol. I
ANL-84-61 Vol. I

2. TITLE AND SUBTITLE
Light-Water-Reactor Safety Fuel Systems Research Programs: Quarterly Progress Report, January--March 1984

3. LEAVE BLANK

4. DATE REPORT COMPLETED
MONTH | YEAR

5. AUTHOR(S)
-

6. DATE REPORT ISSUED
MONTH: September | YEAR: 1984

7. PERFORMING ORGANIZATION NAME AND MAILING ADDRESS (Include Zip Code)
Argonne National Laboratory
9700 South Cass Avenue
Argonne, Illinois 60439

8. PROJECT/TASK/WORK UNIT NUMBER

9. FIN OR GRANT NUMBER
A2016, A2017

10. SPONSORING ORGANIZATION NAME AND MAILING ADDRESS (Include Zip Code)
Division of Accident Evaluation
Office of Nuclear Regulatory Research
U. S. Nuclear Regulatory Commission
Washington, D. C. 20555

11a. TYPE OF REPORT
Technical

b. PERIOD COVERED (Inclusive dates)
January--March 1984

12. SUPPLEMENTARY NOTES

13. ABSTRACT (200 words or less)

This progress report summarizes the Argonne National Laboratory work performed during January, February, and March 1984 on water reactor safety problems related to fuel and fuel cladding materials. The research and development areas covered are Transient Fuel Response and Fission Product Release and Clad Properties for Code Verification.

14. DOCUMENT ANALYSIS - a. KEYWORDS/DESCRIPTORS
fission product modeling
fission product release
irradiated Zircaloy cladding
mandrel loading tests
Zircaloy fracture
Zr_3O precipitation

b. IDENTIFIERS/OPEN-ENDED TERMS

15. AVAILABILITY STATEMENT
Unlimited

16. SECURITY CLASSIFICATION
(This page) unclassified
(This report) unclassified

17. NUMBER OF PAGES
44

18. PRICE